Soft Matter

PAPER

Check for updates

Biomechanical fracture mechanics of composite layered skin-like materials

Christopher H. Maiorana, Rajeshwari A. Jotawar and Guy K. German (iD) *

Most protective biological tissues are structurally comprised of a stiff and thin outer layer on top of a soft underlying substrate. Examples include mammalian skin, fish scales, crustacean shells, and nut and seed shells. While these composite skin-like tissues are ubiquitous in nature, their mechanics of failure and what potential mechanical advantages their composite structures offer remains unclear. In this work, changes in the puncture mechanics of composite hyperelastic elastomers with differing non-dimensional layer thicknesses are explored. Puncture behavior of these membranes is measured for dull and sharp conical indenters. Membranes with a stiff outer layer of only 1% of the overall composite thickness exhibit a puncture energy comparable to membranes with a stiff outer layer approximately 20 times thicker. This puncture energy, scaled by its flexural capacity, achieves a local maximum when the top layer is approximately 1% of the total membrane, similar to the structure of numerous mammalian species. The mode of failure for these regimes is also investigated. In contrast with puncture directly beneath sharp tips caused by high stress concentrations, a new type of 'coring' type fracture emerges at large indentation depths, resulting from accumulated tensile strain energy along the sides of the divot as the membrane is deformed with a blunt indenter. These results could enhance the durability and robustness of stretchable materials used for products such as surgical gloves, packaging, and flexible electronics.

Introduction

Nature offers a variety of integumentary systems that are comprised of a thin and mechanically stiff superficial tissue layer that imparts protection to a more compliant and fragile underlying tissue. These materials range from the armor-like scales of fish[1,2] to the outermost epidermal layer of mammalian skin.[3] The exact role and function of such barriers is a topic of contemporary interest for the biomechanics and biomimicry community, as well as experimental biologists who have sought to better understand the possible roles biological subsystems play in the overall function of an organism.[4–7] Outside of nature, brittle gels and polymers are often used for protective packaging because of their toughness, flexibility, and ability to retain their shape without plastically deforming. Practical applications such as these can often lead to large magnitude complex deformations such as out of plane bending and twisting.[8,9] Thus, these deformations are not limited to simple tensile or compressive loading conditions.

Puncture of soft materials and rubber membranes has been the subject of several investigations[10–13] to better understand the modes of failure and mechanical limits of these materials, of relevance not only to materials science, but also to the packaging and biomedical device industries. Many of these studies investigate predictive models describing contact force-displacement behavior during indentation, originating with Hertzian contact mechanics.[14] The accuracy of these models however is often restricted to shallow indentation depths, typically to ensure deformation of these hyperelastic materials remains small and within the linear regime of the material. However biological and bioinspired materials are commonly nonlinear and can undergo large deformations.[15,16] This makes predictive models based on minute perturbations or small deformations invalid. Moreover, biological systems also have complex composite intrinsic structures, commonly comprised of discrete material layers, each possessing their own hetero-geneous composition and mechanical properties. Along with these structural variations, intrinsic and extrinsic factors such as ageing or solar irradiation further make their mechanical responses difficult to predict.[17,18]

Indentation of soft membranes and bilayers has been explored by several groups,[19–22] however most studies of elastic bilayers continue to focus on shallow indentation depths. Penetration depths required for rupture of compliant hyperelastic materials can however be notably large. Indentation of an elastic half space has been considered by Boussinesq,[23] Sneddon,[24] and Harding.[25]

Department of Biomedical Engineering, Binghamton University, 4400 Vestal Parkway East, Binghamton, NY 13902, USA. E-mail: ggerman@binghamton.edu; Tel: +1 (607) 777-4270

However, these solutions are unlikely to be applicable to multi-layered composites with heterogeneous mechanical properties. In addition to the aforementioned complications of multilayered systems, tissues in biology often contain additional complexities such as vessels filled with fluid or liquid volumes that are also subject to any applied deformation. The topic of how a flexible sheet deforms on top of a fluid has also been explored by several groups.[26–28] What is lacking is an understanding of deep indentation and puncture mechanics of composite hyperelastic membranes and how variations in the relative thickness ratio of the 'stiff-on-soft' composite skin membrane changes puncture behavior. These aspects are considered in this here.

Methods

Fabrication of layered elastomer membranes for puncture

A silicone elastomer was prepared by mixing a base (Sylgard 184, Dow Corning, Midland, MI) with the curing agent in a weight ratio of $55:1$. After the elastomer was mixed and degassed, it was poured into a glass beaker (VWR, Radnor) containing 80 mL of pure glycerin (Sigma-Aldrich, St. Louis). The immiscibility of the glycerin and elastomer mixture prevented the cured elastomer from becoming bonded to the glass bottom of the beaker, and ensured the formation of a flat membrane. The mixture was then degassed in a vacuum dessicator and cured overnight at 60 °C for 12 h. A second elastomer with either a $5:1$ or $55:1$ base to curing agent ratio was prepared along with the addition of blue silicone pigment in order to distinguish between the two elastomer layers (Silc Pig, Smooth-On, Macungie, PA). Aside from the pigment, the second elastomer was prepared in the same manner as previously described, then poured over the first elastomer membrane, degassed, and then cured for 12 h at 60 °C. After curing, the composite elastomer membrane was adhered only to the sides of the breaker, without any air pockets in the glycerin. After mechanical indentation testing, membranes were debonded from the beaker using a scalpel, and sectioned using a flat edged razor blader. Bright-field microscopy (Nikon Eclipse Ti-U, Nikon, Melville) with a $1\times$ objective lens and 0.4 numerical aperture was used to measure the thickness of the dyed layer and the undyed layer as well as the overall thickness of each sample. The necessary volumes were obtained by extrapolating the volume used for early preliminary samples and the corresponding final thickness obtained. The $5:1$ and $55:1$ layers respectively exhibit an elastic modulus of $E = 16$ kPa and $E = 1.48$ MPa,[29,30] chosen to be as widely varying as possible for this elastomer.

Fabrication of large layered elastomer membranes for strain quantification

Thin skinned composite membranes were created by mixing a base (Sylgard 184, Dow Corning, Midland, MI) with its curing agent in weight ratio of $55:1$. After mixing and degassing, the elastomer was poured into a custom made 100 mm diameter circular ring with a plexiglass base containing 20 mL of glycerin

(Sigma-Aldritch, St. Louis) which prevented bonding of the cured elastomer to the plexiglass bottom and allowed for easier removal of elastomer. The mixture was then degassed and cured overnight at 60 °C for at least 12 h. A second elastomer with a curing agent in weight ratio of $5:1$ and was mixed with 0.25 mL of fluorescent silicone pigment (Silc Pig Electric, Smooth-On, Macungie, PA) then prepared in the manner as previously described. The flourescent elastomer was deposited by dipping the tip of a 10 μL pipette tip into the mixture and then lightly contacting the surface of the cured elastomer, leaving a ~ 1 mm diameter circular mark on the surface. The flourescent elastomer was then cured for 15 min at 90 °C. A third elastomer was prepared with curing agent in weight ratio of $5:1$ in the same manner as previously described, then poured onto the membrane surface, and allowed to spread until the entire surface of the membrane was covered with uniform thickness, then cured at 60 °C for 1 h.

For homogenous stiff membranes a silicone elastomer was prepared by mixing a base (Sylgard 184, Dow Corning, Midland, MI) with the curing agent in weight ratio of $5:1$. After being mixed and degassed, the elastomer was poured into the custom circular ring with a plexiglass base containing 20 mL of glycerin (Sigma-Aldrich, St. Louis). The mixture was then degassed and cured overnight at 60 °C for at least 12 h. The second flourscent elastomer with a curing agent in weight ratio of $5:1$ and was mixed with 0.25 mL of fluorescent silicone pigment (Silc Pig Electric, Smooth-On, Macungie, PA) then prepared and deposited in the manner as previously described. A third elastomer was prepared with curing agent in weight ratio of $5:1$ in the same manner as previously described, then approximately 1.2 g was poured onto the membrane surface, and allowed to spread until the entire surface of the membrane was covered, then cured at 60 °C for 1 h.

Once all elastomer layers were was fully cured, the aluminium ring with the adhered membrane was separated from the base containing the glycerol and then rinsed and dried. Membranes used to quantify strains did not have a glycerol layer underneath during testing.

After mechanical indentation testing, the samples were removed from the beaker and sectioned with a razor blade. The thickness of the dyed layer and the undyed, as well as the overall thickness of each membrane sample was measured in all cases using bright-field microscopy (Nikon Eclipse Ti-U, Nikon, Melville) with a $1\times$ objective lens and 0.4 numerical aperture.

Puncture experiments

Having cured PDMS membranes with density, $\rho = 965$ kg m^{-3}, on immiscible glycerin with a density,[31] $\rho = 1258.9$ kg m^{-3}, the membranes are assumed to cure in a stress free state without notable gravitational effects distorting the film. Samples were indented with needles (W. W. Grainger Inc., Lake Forest) with radii of curvature, $r = 0.33$ (results in Fig. 1–5 and 6b) and $r = 0.15$ mm (results in Fig. 2–5). One of two mechanical tensometers were used to perform puncture experiments. Most membranes were indented using a tensometer with 250 N load cell (CellScale Univert, Waterloo, Canada). However, due to the
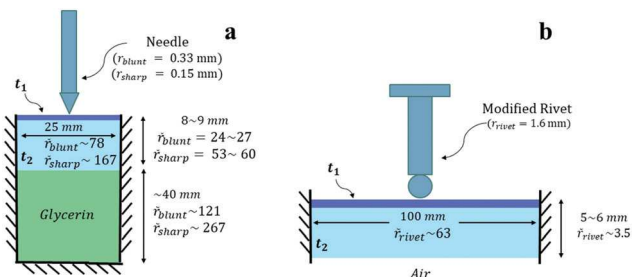
Fig. 1 Composite membrane experimental setup. Schematics displaying experimental set up for puncturing (a) small and (b) large membranes. The radii of the two needles used in the smaller samples experiments and the radii of the modified rivet are denoted as r_{blunt}, r_{sharp}, and r_{rivet}, respectively. The width and thickness of both types of membranes are listed in units of mm as well as nondimensionalized values normalized by the corresponding indenter radius. For more information regarding the data collected from these experiments please refer to the Methods section of the text.
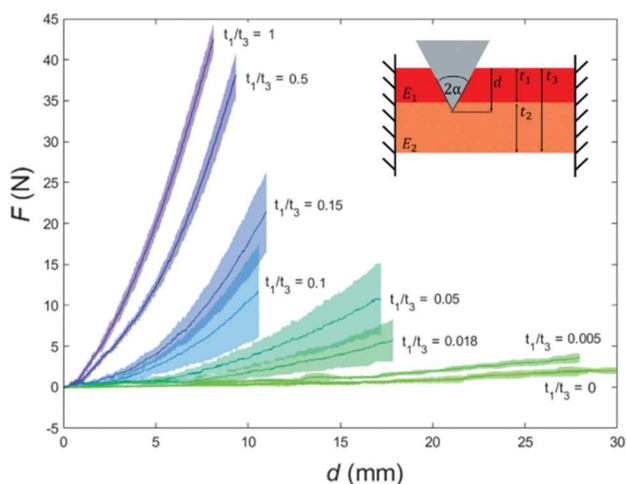

Fig. 2 Composite membrane puncture profiles. Average force *vs.* displacement profiles up until puncture for composite dual layer membranes indented with an indenter of tip radius of curvature $r = 0.33$ mm and half angle $\alpha = 45°$ for varying values of t_1/t_3. Shaded regions represent sample standard deviations of each t_1/t_3 group ($t_1/t_3 = 0$: $n = 3$ samples, $t_1/t_3 = 1.0$, 0.5, 0.05, & 0.018: $n = 4$ samples, $t_1/t_3 = 0.15$, 0.005: $n = 5$ samples, and $t_1/t_3 = 0.1$: $n = 7$ samples. Force values for each group are plotted until the minimum fracture depth for that group. (inset) Schematic representation of the indentation experiment.

significantly lower force response of the thin skinned membranes, a tensometer with 4 N load cell (CellScale Ustretch, Waterloo, Canada) was employed. In the case of the larger samples used for strain quantification, a modified rivet (W. W. Grainger Inc., Lake Forest) with a spherical head with $r = 1.6$ mm (results in Fig. 6a and 7, 8) was used. The samples were indented at a velocity of 0.08 mm min^{-1}. Force displacement curves were obtained until rupture through the entire membrane thickness. No debonding of the membrane from the side of the glass beaker occurred prior to rupture. Membranes consistently ruptured away from the base of the glass beaker.

Cross sectional imaging of punctured membrane layer thickness

Membranes were sectioned after puncture using a paper trimmer (Swingline, Lincolnshire, IL). Cut planes of each section were oriented orthogonal to the local fracture plane. Individual sections were placed on a glass coverslip, mounted on an inverted microscope (Nikon Eclipse Ti-U, Nikon, Melville) with $1\times$ objective lens, and imaged in brightfield using a CCD camera (Andor Clara. Belfast, Northern Ireland). The thicknesses of the two individual composite layers were identified *via* differences in color between the dyed and undyed elastomer.

Membrane imaging and strain quantification for puncture experiments

During indentation, large membranes with a thin stiff skin layer comprising less than 3% of the total membrane thickness were imaged at a frequency of 30 Hz using a dermal camera (DE 300 Digital Dermatoscope, Firefly, Belmont, MA). Local material deformations were captured at a resolution of 81.25 µm per pixel (720 × 480 pixels). To enable tracking of localized strains, regions of the membranes were infused with fluorescent pigment and illuminated with 365 nm narrowband light using an ultraviolet lamp (8 Watt EL Series, Analytik Jena US LLC, Upland, CA). Spatially resolved 2D displacements along the
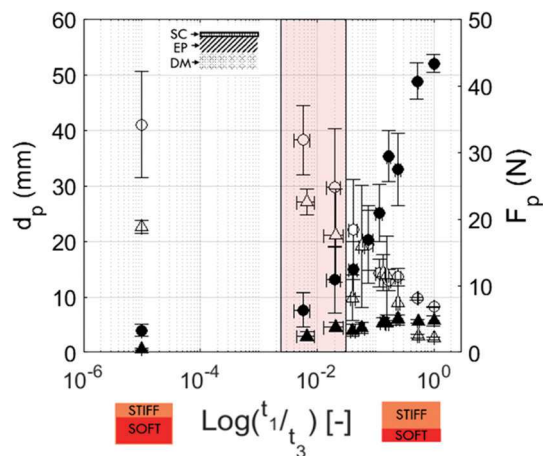

Fig. 3 (a) Puncture depth (d_p, open symbols) and (b) puncture force (F_p, filled symbols) as a function of t_1/t_3. Vertical error bars denote standard deviations of $n \geq 4$ individual samples. Horizontal error bars denote the standard deviation in t_1/t_3 within the group. Circles indicate samples tested with an indenter radius of curvature of 0.33 mm and $\alpha = 45°$. Triangles indicate samples tested with an indenter radius of curvature of 0.15 mm and $\alpha = 15°$. The data points for $t_1/t_3 = 0$ are treated as $t_1/t_3 = 1 \times 10^{-5}$ so that they are visible on the logarithmic axis. The shaded region indicates the biologically relevant "skin zone", which encompasses the t_1/t_3 values for murine, leporine, porcine, and human skin tissue. Data points show average values of $t_1/t_3 = 0$: $n = 3$ independent samples, $0.03 < t_1/t_3 \leq 0.05$, $0.15 < t_1/t_3 \leq 0.20$, $0.20 < t_1/t_3 \leq 0.30$, $t_1/t_3 = 0.5$, and $t_1/t_3 = 1.0$: $n = 4$ samples, $0.05 < t_1/t_3 \leq 0.10$: $n = 8$ samples, $0.01 < t_1/t_3 \leq 0.03$ and $0.10 < t_1/t_3 \leq 0.15$: $n = 9$ samples, $t_1/t_3 \leq 0.01$: $n = 12$ samples. The shaded biologically relevant values were calculated by dividing the reported thickness of the stratum corneum by the total epidermal and dermal tissue thickness from literature.[33,34]
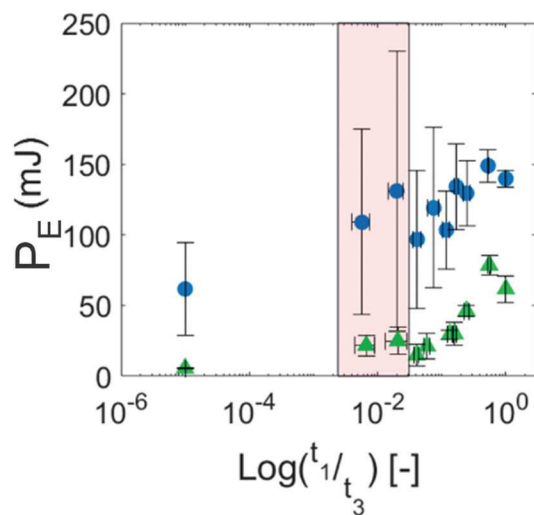
Fig. 4 Puncture energy, P_E, as a function of composite membrane thickness ratio, t_1/t_3. Vertical error bars denote standard deviations of P_E for $n \geq 4$ independent samples. Horizontal error bars denote the standard deviation of t_1/t_3 within that group. Solid blue circles indicate samples tested with an indenter radius of curvature of 0.33 mm and $\alpha = 45°$. Green triangles indicate samples tested with and indenter radius of curvature of 0.15 mm and $\alpha = 15°$. The data points for $t_1/t_3 = 0$ are treated as $t_1/t_3 = 0.001$ so that they are visible on the logarithmic axis. Data points show average values of t_1/t_3 groups ($t_1/t_3 = 0$: $n = 3$ samples, $0.03 < t_1/t_3 \leq 0.05$, $0.15 < t_1/t_3 \leq 0.20$, $0.20 < t_1/t_3 \leq 0.30$, $t_1/t_3 = 0.5$, and $t_1/t_3 = 1.0$: $n = 4$ samples, $0.05 < t_1/t_3 \leq 0.10$: $n = 8$ samples, $0.01 < t_1/t_3 \leq 0.03$, $0.10 < t_1/t_3 \leq 0.15$: $n = 9$ samples, and $t_1/t_3 \leq 0.01$: $n = 12$ samples). The shaded biologically relevant skin zone is established by dividing the reported thickness of the animal stratum corneum by the total thickness of the epidermis and dermis.[33,34]

membrane width were quantified with single pixel resolution using a centroid tracking algorithm.[32] The longitudinal positions of centroids along the long axis of the membrane were used to establish displacements. Local strains were established from centroid pairs using the expression, $\gamma_{x,ij} = (\vec{u_i} - \vec{u_j})/\overrightarrow{x_i} - \overrightarrow{x_j}$, where $\vec{u}$ and $\vec{x}$ respectively denote the longitudinal displacement and position vectors of centroids i & j. Individual pair strains were calculated for the region beneath the indenter head and either side of the indenter.

Statistical analysis

Statistical analyses were performed using R Version 3.4.2. To assess for normality and homoscedasticity, Shapiro-Wilke's and Levine's test were performed for all data sets. Statistical significance was found using a one-way analysis of variance (1-way ANOVA or in some cases a two sample t-test. The F-value for each test is denoted in the corresponding figure caption. *Post hoc* analyses were performed when statistical significance was established to determine which specific groups within the dependent variable were most significant. In the figures, * denotes $p \leq 0.05$, ** denotes $p \leq 0.01$, and *** denotes $p \leq 0.001$.

Biologically relevant "skin zone" approximation

Thickness measurements for the stratum corneum, t_1, and full skin thickness (comprising the epidermis and dermis), t_3, of
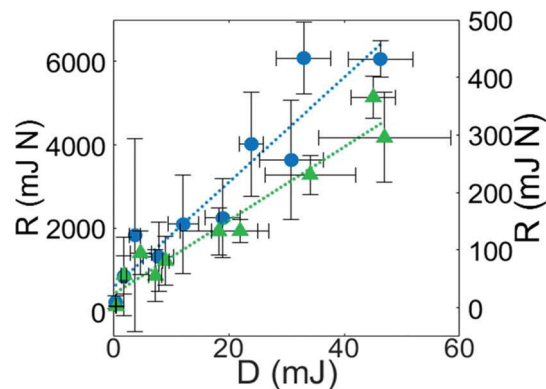

Fig. 5 Puncture resistance, R, as a function of flexural rigidity, D, for each t_1/t_3 group. Data points show averages of t_1/t_3 groups ($t_1/t_3 = 0$: $n = 3$ samples, $0.03 < t_1/t_3 \leq 0.05$, $0.15 < t_1/t_3 \leq 0.20$, $0.20 < t_1/t_3 \leq 0.30$, $t_1/t_3 = 0.5$, and $t_1/t_3 = 1.0$: $n = 4$ samples, $0.05 < t_1/t_3 \leq 0.10$: $n = 8$ samples, $0.01 < t_1/t_3 \leq 0.03$, $0.10 < t_1/t_3 \leq 0.15$: $n = 9$ samples, and $t_1/t_3 \leq 0.01$: $n = 12$ samples). Values on the left-hand y-axis correspond to the solid blue circles and denote results of samples tested with an indenter radius of curvature of 0.33 mm and $\alpha = 45°$. Values on the right-hand y-axis correspond to the solid green triangles and denote samples tested with and indenter radius of curvature of 0.15 mm and $\alpha = 15°$. Horizontal error bars denote the standard deviation in t_1/t_3 within that group. The R^2 values for the blunt tip and sharp tip are 0.944 and 0.968 respectively, with goodness of fit p-values of 4.10×10^{-5} and 4.65×10^{-6}.
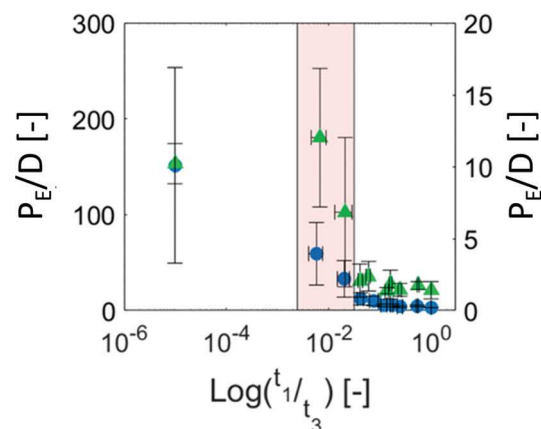

Fig. 6 Puncture energy, P_E, scaled by flexural rigidity, D, as a function of t_1/t_3. Data points show averages of t_1/t_3 groups ($t_1/t_3 = 0$: $n = 3$ samples, $0.03 < t_1/t_3 \leq 0.05$, $0.15 < t_1/t_3 \leq 0.20$, $0.20 < t_1/t_3 \leq 0.30$, $t_1/t_3 = 0.5$, and $t_1/t_3 = 1.0$; $n = 4$ samples, $0.05 < t_1/t_3 \leq 0.10$:$n = 8$ samples, $0.01 < t_1/t_3 \leq 0.03$ and $0.10 < t_1/t_3 \leq 0.15$: $n = 9$ samples, and $t_1/t_3 \leq 0.01$: $n = 12$ samples). Values on the left-hand y-axis correspond to the blue circular marker symbols, which indicate samples tested with an indenter radius of curvature of 0.33 mm and $\alpha = 45°$. Values on the right-hand y-axis correspond to the green triangular marker symbols, which indicate samples tested with and indenter radius of curvature of 0.15 mm and $\alpha = 15°$. Horizontal error bars denote the standard deviation in t_1/t_3 within that group. The shaded biologically relevant skin zone range reports the thickness of the animal stratum corneum scaled by the total thickness of the epidermis and dermis from for murine, leporine, porcine, and human skin tissue.[33,34]

humans, mice, pigs, and rabbits were taken from previously published data.[33,34] The corresponding lower bound of
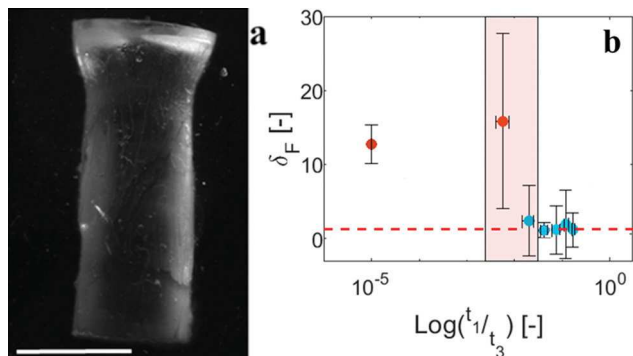
Fig. 7 (a) A representative cylindrical core. The composite membrane sample was indented with a spherically headed indenter with a diameter of 3.2 mm, the scale bar indicates 2 mm. (b) Dimensionless mean fracture distance away from the indenter tip scaled by the probe tip radius, δ_F, as a function of t_1/t_3, plotted on a semi-log axis. Data points show averages of t_1/t_3 groups ($t_1/t_3 = 0$: $n = 3$ samples, $0.03 < t_1/t_3 \leq 0.05$, $0.15 < t_1/t_3 \leq 0.20$, and $0.20 < t_1/t_3 \leq 0.30$: $n = 4$ samples. $0.05 < t_1/t_3 \leq 0.10$: $n = 8$ samples, $0.01 < t_1/t_3 \leq 0.03$ and $0.10 < t_1/t_3 \leq 0.15$: $n = 9$ samples, $t_1/t_3 \leq 0.01$: $n = 12$ samples). The shaded biologically relevant skin zone values are calculated by dividing the reported thickness of the stratum corneum by the total thickness of the epidermis and dermis from literature.[33,34] Horizontal error bars denote the standard deviation in t_1/t_3 within that group. Samples are tested with an indenter radius of curvature of 0.33 mm and $\alpha = 45°$. Blue markers indicate averages of less than 1 mm and red markers indicate means greater than 1 mm. The dashed red line indicates $\delta_F = 1$.

biologically relevant t_1/t_3 values is established by scaling the smallest stratum corneum thickness by the largest overall combined thickness, while the upper bound denotes the largest stratum corneum thickness scaled by the smallest overall combined thickness.

Results and discussion

In this study, the indentation and puncture mechanics of hyperelastic composite 'stiff-on-soft' two layer skin membranes are studied. These membranes are comprised of a stiff outer layer adhered to an underlying softer substrate, analogous to the common structure of the integumentary system in the animal kingdom. The elastic modulus of each layer is maintained throughout experimentation, such that changes in the mechanical properties of the composite membranes result only from alterations of the fractional thickness of the stiff outer skin layer scaled by the total composite skin thickness, t_1/t_3, as shown in the schematics of Fig. 1 and 2. For small and large membrane indentation studies, t_3, was held constant. The composite membranes in each case are cured over a volume of immiscible glycerin, leaving only their outer perimeter adhered to the sides of the vial. This also enables exploration of greater membrane puncture indentation depths and full puncture phenomena. The organization of the membrane and indenter probe is shown schematically in Fig. 2. In addition, the glycerin also provides a more physiologically relevant environment for testing the mechanics of soft biological skin
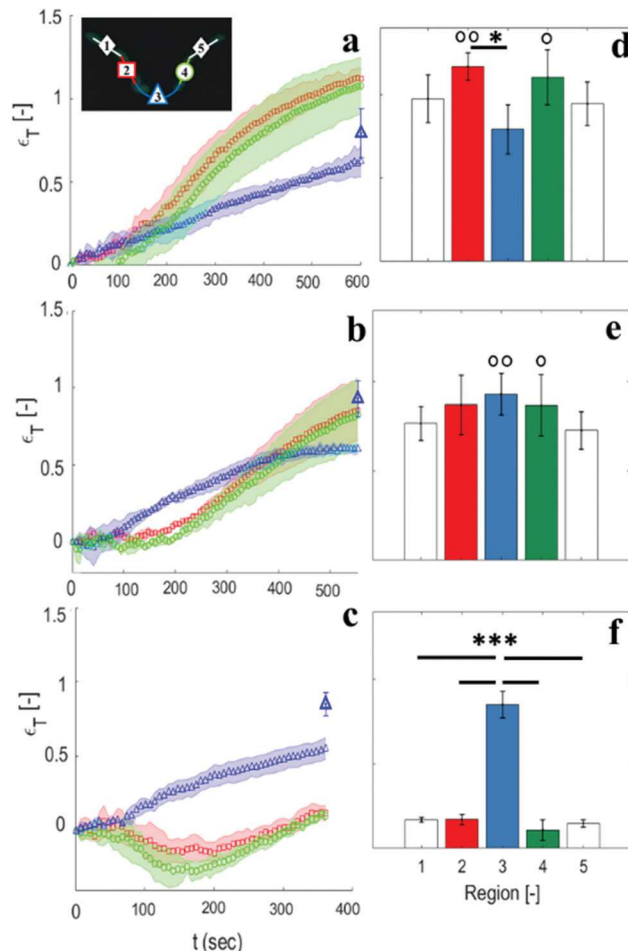

Fig. 8 (a–c) Average true engineering strain, ε_T, within a transect of an indented composite plotted against time, t, for regions 2, 3, and 4 shown in the inset schematic. Region 3 denotes regions directly beneath and in contact with the indenter. Regions 2 and 4 denote regions either side of the indenter that are not in contact with the indenter. Panels correspond to the behavior of: (a and d) unlubricated composite membranes with $t_1/t_3 \leq 0.03$, (b and e) lubricated thin skinned membranes with $t_1/t_3 \leq 0.03$, and (c and f) unlubricated homogenous stiff membranes with $t_1/t_3 = 1$. Shaded regions indicate the standard deviations of $n = 3$ individual samples. Red squares, blue triangles, and green circles represent the strains in regions 2, 3, and 4 respectively. The larger blue triangles represent the adjusted final true strain in region 3, accounting for the curvature of the membrane around the indenter. Error bars indicate the standard deviations of $n = 3$ samples. (d–f) Average true engineering strains in each region immediately prior to rupture. Error bars indicate standard deviations of $n = 3$ different samples. Unfilled circles indicate where fracture is initiated for each tested sample. P-Values are established using a 1-way ANOVA and Tukey's multiple comparisons test obtaining F-values of 3.46, 1.14 and 40.80 for (d)–(f) respectively.

tissue analogs, which typically sit on top of highly deformable viscoelastic underlying organs or adipose tissue.[3]

Fig. 2 shows that notable changes to the puncture depth, d_p, and puncture force, F_p, occur with changes in the composite structure of the membranes, accomplished by varying t_1/t_3. While homogeneous membranes comprised entirely of the stiff, $E = 1.48$ MPa, outer skin layer, $t_1/t_3 = 1$, exhibit steep slopes, large puncture forces, and small puncture depths,

membranes comprised entirely of the soft (E = 16 kPa) lower layer material, t_1/t_3 = 0, exhibit notably smaller puncture forces and notably larger puncture depths. A clear and near monotonic transition between these two types of behavior occurs as t_1/t_3 decreases from very thick stiff outer layer ($t_1/t_3 \sim 1$) to a very thin stiff outer layer $t_1/t_3 \sim 0$). In all cases the force response is briefly linear before transitioning to a hyperelastic Neo–Hookean response, similar to previous observations.[35–38]

The mechanical deformability of thinner skinned membranes becomes more apparent when the puncture depth and force are plotted in Fig. 3. To explore the effects of the indenter tip geometry, puncture data is collected using two different needles. Regardless of tip dimensions, puncture depths increase as t_1/t_3 decreases. This illustrates that one potential mechanical advantage for thinner skinned biological systems is that thin skinned materials are notably more accommodating to out of plane forces than those with thicker skins. For the blunter probe, the applied forces are distributed over a larger contact area, thereby reducing the stress intensity directly underneath the tip. As alluded to by Fakhouri et al.,[39] this change in failure could potentially result from the large contact area pushing the failure mode from an energy limited regime to a stress limited regime. A stress limited regime occurs when the amount of strain energy in the material surrounding the crack plane has already reached a critical nucleation point, therefore depending only on the stress reaching the maximum cohesive stress required to physically break the material. The energy limited case is the opposite. The cohesive stress criterion beneath the indenter has already been met, however the amount of energy in the surrounding material required to perform the work to create the new interface has not yet risen to the critical nucleation energy. A clear transition in puncture force occurs in Fig. 3 at $10^{-3} \leq t_1/t_3 \leq 10^{-2}$. Membranes with $t_1/t_3 \leq 10^{-3}$ show only a slow increase in F_p with increasing t_1/t_3. However, for $t_1/t_3 > 10^{-2}$, F_p increases rapidly and logarithmically with t_1/t_3. The sharper probe, by contrast, has a much smaller contact area, resulting in the forces being more concentrated. We anticipate that this leads to a more intense and rapid buildup of localized stress, resulting in shallower puncture depths. While the overall trends in puncture depth between the two needles are similar, the trends in puncture forces are noticeably different. In the case of the blunt probe, F_p decreases sharply as t_1/t_3 decreases. In comparison, the puncture force rises only moderately for the sharp probe tip, increasing by $\sim$1 N to a plateau of 3–4 N as t_1/t_3 increases. In terms of the biologically relevant skin zone, it appears that in the case of a sharper indenter, the puncture depth for thin skinned membranes ($t_1/t_3 \leq 0.03$) is maximized while the puncture force remains similar to a far thicker skin. For the blunter probe, the skin zone falls around the transition between shallow and rapid increases in F_p with t_1/t_3. This transition signifies that both puncture depth and puncture force are concurrently maximized.

Changes in the puncture energy, $P_E = \int_0^{u_p} F(\vec{u})\mathrm{d}u$, required to completely puncture the material with t_1/t_3 are also examined by quantifying the area under indentation force, $F(\vec{u})$, vs.

displacement, $\vec{u}$, curves, where u_p denotes the puncture displacement. These are displayed in Fig. 4. Here the energetic cost of fracture increases with the size of the probe tip, in agreement with previous findings. Indentation using a probe tip with a small radius of curvature leads to shallower puncture depths, and lower puncture forces, resulting in reduced puncture energy costs. As the size of the probe tip increases, the deformation zone became larger, resulting in the elastic energy becoming dispersed over broader areas. In contrast, smaller radius of curvature tips result in elastic energy localized to a smaller region surrounding the probe. In general, for the blunt probe tip, when $0.01 \leq t_1/t_3 \leq 1$, the mean puncture energy fluctuates but remains similar with $100 \leq P_E \leq 150$ mJ. This is likely due to the fracture force and the fracture depth exhibiting an approximately inversely proportional relationship. In the case of the sharp tip, two clear regimes are observed; a high energy regime when $t_1/t_3 \geq 0.2$, and a low energy regime when $t_1/t_3 < 0.2$. While the puncture energy increases logarithmically with increasing t_1/t_3 in the high energy regime, it remains relatively uniform in the low energy regime. From a biological perspective, changes in t_1/t_3 for puncture with a blunt probe tip offer no mechanical advantage in skin strength. With respect to the sharper needles, the puncture of a thicker skin ($t_1/t_3 \geq 0.2$) is a maximum of 3–4 times more energetically costly. However, it is possible that within the physiologically relevant skin zone, the skin structure is maximizing the energetic cost of rupture while concurrently minimizing the volume space of the stiff superficial skin layer.

To further characterize composite membrane strength, the puncture resistance is quantified. Previous studies report that for sharper indentation probes, puncture resistance is an accurate measure of damage resistance.[40,41] The puncture resistance, $R = P_E F_p$, is the product of the puncture energy and the puncture force. However, we anticipate that an increase in the outer stiff skin layer thickness will notably alter the flexibility of the membrane. The ability to bend and stretch the exterior layer of skin tissue are important traits for most terrestrial and volant mammals.[42,43] As such, the rigidity, $D = [E_1(t_1^3 + 3t_1t_2^2) + E_2(t_2^3 + 3t_1^2t_2)]$, of each membrane is also quantified, where E_1 and t_1 are respectively the elastic modulus and thickness of the stiff superficial layer and E_2 and t_2 are the complementary parameters of the softer underlying substrate layer.[44–46] Fig. 5 shows that a positive linear trend between puncture resistance and membrane rigidity exists for both indenter radii of curvature. While this result appears both plausible and logical; an increase in the stiff outer skin layer thickness increases damage resistance and reduces the flexibility of the barrier, the empirical cost of achieving a greater puncture resistance is flexurally expensive. The average puncture resistance of the thinnest skinned composite membranes with $t_1/t_3 < 0.01$ ($D \sim 3$ mJ) fall equal to or below $\sim$2000 mJN. To achieve an average puncture resistance at least double this value, the flexural rigidity of the membrane must increase beyond 25 mJ for both the sharp and blunt indenters, approaching an order of magnitude increase. To further highlight this, P_E/D, is plotted as a function of t_1/t_3 in Fig. 6. Both the

indenter types display relatively constant P_E/D values which then show notable increases once t_1/t_3 decreases below 0.03. This reveals that membranes that fall within the biologically relevant 'skin zone' range are particularly effective in maximizing the energetic cost of rupture while remaining as flexible as possible. Values of P_E/D for the blunt indenter are also maximized in this zone.

Puncture of thin skinned ($t_1/t_3 \ll 1$) composite membranes with a blunt indenter is associated with large values of P_E/D. It is also associated with a change in the mode of failure. These highly deformable membranes require large probe indentation depths to induce rupture, forming a divot whose depth notably exceeds the membrane thickness. During indentation, while the membrane underneath the probe tip is expected to undergo a compressive strain, the region delineated by the membrane outer edge and the loci where the membrane loses contact with the probe, will undergo tensile strain. For the case of a blunt tip, rupture does not occur below the indenter probe. Rather, an axisymmetric rupture at a fixed distance away from the probe occurs, resulting with a cylindrical core separating from the membrane. To the author's knowledge, this phenomenon has not previously been observed. Rather than puncture of the membrane beneath the indenter tip, the new rupture pattern we denote as membrane 'coring'.

The likeliest cause of this coring type failure is a localized strain energy beneath the probe tip smaller than that further from the indenter, with coring initiated when the strain energy at a localized position surpasses the characteristic fracture nucleation energy of the material. A representative cylindrical core of material in shown Fig. 7a. This core forms as a result of a crack propagating circumferentially at a near fixed radial position from the indenter tip, as well as through the total membrane thickness, orthogonal to the induced tensile strain. Fracture is observed to initiate in the stiff outer layer. However, while fracture will develop into the thicker underlying substrate with a lower elastic modulus and greater fracture strain,[18,47] this transition is anticipated to cause a more blunted crack, mitigating the stresses present at the crack growth front.[48] As the crack proceeds through the substrate, the cracking through the thin and stiff outer skin layer occurs rapidly, resulting in the preliminary radial ''core' morphology, which propagates through the depth of the membrane. Similar circumferential fracture morphologies have been observed.[49,50] Liu *et al.*[49] attribute this morphology to the effect of friction. However, this effect has only been investigated in the case of thin homogenous membranes. If this behavior is primarily frictionally driven, then the fracture distance away from the indenter tip would be expected to approximately correspond with the edges of the contact area. To characterize the transition to this new failure regime, the average distance away from the indenter tip where circumferential fracture originates, normalized by the radius of the indenter probe, δ_F, is plotted against t_1/t_3 in Fig. 7b. While fracture in membranes with $t_1/t_3 \geq 0.03$ occurs beneath the indenter, fracture initiates far beyond $\delta_F = 1$ as t_1/t_3 becomes small. As shown in Fig. 8, radial membrane strains in proximity to the probe reach $\gamma_{rr} \approx 1$, suggesting that if

frictional effects were the cause of this failure, the core diameters when measured in their unstrained state should not exceed $\delta_F \approx 0.5$. The average size of the measured cores being $\delta_F \gg 1$ for small values of t_1/t_3 indicates rupture is unlikely to be associated with frictional effects. Within the shaded skin zone, the mean fracture distance transitions from approximately $\delta_F = 1$ to an average of $\delta_F \approx 15$, indicating a transition from direct membrane puncture to a coring type failure.

To better understand how coring fracture occurs, one dimensional strain transects within thin skinned membranes with $t_1/t_3 \leq 0.03$ are established. Transects are made across the diameter of the membrane and include strains in vicinity and beneath the probe tip during indentation. A schematic of transect locations is displayed in the inset diagram in Fig. 8a. The average true strain, $\varepsilon_T = \ln(L_F/L_0)$, is plotted against time in Fig. 8a–c for three different indentation scenarios, where L_F and L_0 are respectively the final and initial length of each transect, all five regions were similar in initial length ($\sim$1–2 mm). Region 3 was marginally smaller ($\sim$1 mm) due to it undergoing significant strains and conforming to the diameter of the indenter. The locations of coring events (open circle symbols) and final true strains (bars) are shown in corresponding Fig. 8d–f.

First, unlubricated thin and stiff outer layer membranes are tested. While initially regions 2, 3, and 4 (regions closest to the probe tip) appear to deform at similar rates, regions 2 and 4, adjacent to and not in contact with the probe tip, increase nonlinearly and ultimately reach larger strains than the central region 3 after approximately 200 seconds. In contrast, strains develop near linearly in region 3. Strains in regions 1 and 5 were consistently the same or lower than those in regions 2–4, as shown in Fig. 8d–f and were near zero in the 100% stiff case Fig. 8(c–f). Just prior to rupture the true strains in regions 2 and 4 are nearly twice that of region 3. However, this does not account for the curvature of the membrane around the indenter. To correct for this, the arc length of region 3 just prior to rupture is measured and used to calculate a final adjusted true strain value. This final adjusted strain is plotted as an enlarged blue triangle in Fig. 8a–c. This more accurate strain is also used for statistical comparison of final true strain values in regions 1–5 just prior to rupture (Fig. 8d–f). The final mean strain in region 3 is statistically lower than that of region 2, but not from region 4, likely due to increased noise in region 4 in one of the experiments. These higher strains correlate with the locations where fracture is initiated.

To further evaluate the impact of frictional effects, previously thought to be the cause of circumferential rupture, thin and stiff outer layer membranes are tested with a lubricant placed directly between the probe tip and membrane. Fig. 8b shows that friction does appear to play a role in reducing strain in regions 2 and 4, while increasing strains in region 3 during indentation. This agrees well with the results observed by Liu *et al.*,[49] where in the absence of a lubricant the sliding of the membrane surface over the indenter is more difficult due to increased interfacial friction.[49] However, even with the application of a lubricant, coring type fracture still occurs, indicating
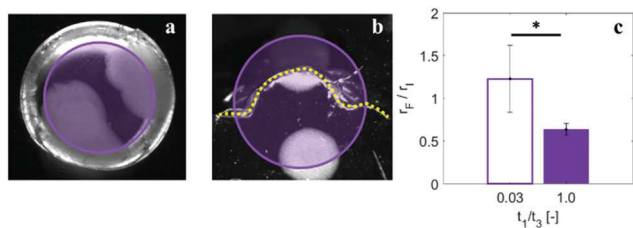
Fig. 9 (a) Plan view of radial core material post fracture for a thin-skinned composite membrane with $t_1/t_3 \leq 0.03$. (b) Plan view of an Ohm-like fracture for a homogenous membrane with $t_1/t_3 = 1$. The yellow dotted line outlines the crack surface. The overlaid circle in (a and b) represents the approximate 3.2 mm diameter of the indenter. (c) Fracture radius, r_f, scaled by indenter radius, r_I, for thin and stiff outer layer membranes with $t_1/t_3 \leq 0.03$ (open bar), and homogeneous single layer membranes with $t_1/t_3 = 1$ (filled bar). Vertical error bars denote standard deviations of $n = 3$ samples. P-Values are established using a one tailed, two sample T-test with a t-value of 2.57.

that a change in rupture type is not exclusively caused by friction and will be affected by sample geometry including the overall membrane thickness and difference in the mechanical properties of the composite layers.

To verify that the heterogeneous composition of the membrane influences rupture behavior, localized strain behavior is quantified in a homogenous membrane with elastic modulus equal to the stiff outer layer of the composite membranes. Notably, not only are strains greatest in the central region 3, but coring failure no longer occurs. Instead "Ohm-like curved cracks" are observed, equivalent to those previously reported by Liu *et al.*[49] in their unlubricated condition. Crack morphologies for the unlubricated thin and stiff outer layer membranes as well as the homogenous stiff membranes are shown in Fig. 9a and b. The mean fracture radius, r_F, normalized by the indenter radius, r_I, for the two membrane types are also compared and shown in Fig. 9c. The dimensionless term, r_f/r_I, is distinct from δ_F (Fig. 7) because r_f/r_I is quantified in an unloaded membrane after fracture occurs, while δ_F is measured in a loaded condition as fracture initiates. Though the statistical variation in r_F/r_I was greater in the composite membranes, the mean is statistically larger than that of the stiff homogenous membranes, indicating that fracture occurs farther way in the case of the thinned skinned composite membranes. The Ohm like fractures occur with $r_F/r_I \approx 0.5$, consistent with the edge of the contact region between indenter and membrane for strains of $\varepsilon_T \approx 1$ (Fig. 8). These patterns in the unlubricated single layer membranes suggest that while circumferential rupture is occurring, a complete transition to coring failure has not occurred, and full coring is only observed in composite membranes.

Results of this study firstly appear to explain how the structure of mammalian skin tissue may have adapted or evolved to exhibit a thin stiff layer on top of a thicker more compliant layer. This morphology provides energetically more advantageous properties with regards to penetration and puncture. Many of the measurements of mammalian skin layer thicknesses, when compared with experimental membrane

equivalents in this study offer local maxima or optimized parameter regimes, in particular concurrent maximization of puncture resistance and skin deformability, essential for offering protection while also enabling efficient climbing, swimming, running, or flying. Further, this optimized structure also offers ample volume for functional living biological tissue beneath the typically terminally differentiated outer skin barrier.[51] Our study further offers insight into the indentation failure mechanics of hyperelastic materials. While the first mode of failure, puncture, is well recognized and relates to the buildup of energy directly below an indenter, this study reveals a second mode, coring, that is associated with the buildup of tensile strains along the sides of the divot at a distance from the indenter. To the author's knowledge, this second type of failure has not been observed previously and could explain observed Ohm-like cracked curves[49] as a transitional type of failure between puncture and coring. We anticipate that the findings of this study provide insight to improve additive manufacturing technology, 3D bioprinting, and nanofabrication techniques[52,53] and opens the door to further investigations into the failure mechanics of composite heterogeneous skin like materials.

Author contributions

C. H. M. and G. K. G. designed the research. C. H. M. and R. A. J. fabricated the samples and performed the mechanical testing. C. H. M. and R. A. J. processed the data. C. H. M. and G. K. G. intrepreted the results and wrote the manuscript.

Conflicts of interest

There are no conflicts to declare.

References

1 M. R. Minicozzi, J. Perez, D. S. Kimball and A. C. Gibb, Scale Thickness Predicts Skin Puncture-Force Resistance in Three Pleuronectiform Fishes, *Integr. Org. Biol.*, 2019, **1**(1), DOI: 10.1093/iob/obz005.

2 R. K. Chintapalli, M. Mirkhalaf, A. K. Dastjerdi and F. Barthelat, Fabrication, testing and modeling of a new flexible armor inspired from natural fish scales and osteoderms, *Bioinspiration Biomimetics*, 2014, **9**(3), DOI: 10.1088/1748-3182/9/3/036005.

3 O. Kuwazuru, J. Saothong and N. Yoshikawa, *Med. Eng. Phys.*, 2008, **30**, 516–522.

4 P. S. L. Anderson, J. Lacosse and M. Pankow, Point of impact: the effect of size and speed on puncture mechanics, *Interface Focus*, 2016, **6**, 20150111.

5 S. N. Patek and R. L. Caldwell, *J. Exp. Biol.*, 2005, **208**, 3655–3664.

6 H. Schwager, T. Masselter, T. Speck and C. Neinhuis, Functional morphology and biomechanics of branch–stem

junctions in columnar cacti, *Proc. R. Soc. B*, 2013, DOI: 10.1098/rspb.2013.2244.

7 C. Chang, P. Wu, R. E. Baker, P. K. Maini, L. Alibardi and C. M. Chuong, *Int. J. Dev. Biol.*, 2009, **53**, 813–826.

8 N. Suksangpanya, N. A. Yaraghi, R. B. Pipes, D. Kisailus and P. Zavattieri, *Int. J. Solids Struct.*, 2018, **150**, 83–106.

9 C. Schumacher, S. Marschner, M. Gross and B. Thomaszewski, Mechanical characterization of structured sheet materials, *ACM Transactions on Graphics*, 2018, **37**(4), DOI: 10.1145/3197517.3201278.

10 C. T. Nguyen and T. Vu-Khanh, *J. Mater. Sci.*, 2004, **39**, 7361–7364.

11 C. T. Nguyen, T. Vu-Khanh and J. Lara, *Theor. Appl. Fract. Mech.*, 2004, **42**, 25–33.

12 C. T. N. T. Vu-khanh, P. I. Dolez and J. Lara, *Int. J. Fract.*, 2009, **155**, 83–91.

13 G. S. Yeh and D. I Livingston., *The indentation and puncture properties of rubber vulcanizates*, 1961.

14 H. Hertz, *J. Reine Angew. Math.*, 1881, **92**, 156–171.

15 J. A. Michel and P. J. Yunker, *Proc. Natl. Acad. Sci. U. S. A.*, 2019, **116**, 2875–2880.

16 E. Rettler, S. Hoeppener, B. W. Sigusch and U. S. Schubert, *J. Mater. Chem. B*, 2013, **1**, 2789–2806.

17 Y. Yuan and R. Verma, *Colloids Surf., B*, 2006, **48**, 6–12.

18 S. Rattan, L. Li, H. K. Lau, A. J. Crosby and K. L. Kiick, *Soft Matter*, 2018, **14**, 3478–3489.

19 B. L. Doss, R. Eliato, K. Lin and R. Ros, *Soft Matter*, 2019, **15**, 1776–1784.

20 F. Box, C. Jacquemot, M. Adda-Bedia and D. Vella, Cloaking by coating: How effectively does a thin, stiff coating hide a soft substrate?, *Soft Matter*, 2020, **16**(19), DOI: 10.1039/c9sm02511a.

21 H. Gao, C. Chiu and J. Lee, *Int. J. Solids Struct.*, 1992, **29**, 2471–2492.

22 C. Jin, A. Davoodabadi, J. Li, Y. Wang and T. Singler, *J. Mech. Phys. Solids*, 2017, **100**, 85–102.

23 J. Boussinesq, *Comptes Rendus*, 1878.

24 I. N. Sneddon, *Int. J. Eng. Sci.*, 1965, **3**, 47–57.

25 B. Y. J. W. Harding and I. N. Sneddon, *Distribution*, 1944, 16–26.

26 F. Box, D. Vella, R. W. Style and J. A. Neufeld, Indentation of a floating elastic sheet: Geometry versus applied tension, *Proc. R. Soc. A*, 2017, **473**(2206), DOI: 10.1098/rspa.2017.0335.

27 T. Fąs, K. Kazimierska-Drobny and M. Kaczmarek, *Acta Mech.*, 2018, **229**, 4779–4790.

28 J. R. Lister, G. G. Peng and J. A. Neufeld, *Phys. Rev. Lett.*, 2013, **111**, 4–8.

29 C. M. Cesa, N. Kirchgeßner, D. Mayer, U. S. Schwarz, B. Hoffmann and R. Merkel, *Rev. Sci. Instrum.*, 2007, **78**, 34301.

30 C. H. Maiorana, M. Erbe, T. Blank, Z. Lipsky and G. K. German, *Sci. Rep.*, 2019, **9**, 1–9.

31 A. Volk and C. J. Kähler, *Exp. Fluids*, 2018, **59**, 1–4.

32 M. Willert and C. E. Gharib, *Exp. Fluids*, 1991, **10**, 181–193.

33 J. C. J. Wei, G. A. Edwards, D. J. Martin, H. Huang, M. L. Crichton and M. A. F. Kendall, *Sci. Rep.*, 2017, **7**, 1–17.

34 M. Geerligs, *Skin layer mechanics*, 2010.

35 I. M. Garnica-Palafox, M. Álvarez-Camacho and F. M. Sánchez-Arévalo, *J. Mater. Sci.*, 2019, **54**, 14255–14274.

36 O. N. Scott, M. R. Begley, U. Komaragiri and T. J. Mackin, *Acta Mater.*, 2004, **52**, 4877–4885.

37 M. Geerligs, L. van Breemen, G. Peters, P. Ackermans, F. Baaijens and C. Oomens, *J. Biomech.*, 2011, **44**, 1176–1181.

38 J. Tan, Y. J. Chao, X. Li and J. W. Van Zee, *J. Fuel Cell Sci. Technol.*, 2009, **6**, 0410171.

39 S. Fakhouri, S. B. Hutchens and A. J. Crosby, *Soft Matter*, 2015, **11**, 4723–4730.

40 J. Lange, H. Mokdad and Y. Wyser, Understanding Puncture Resistance and Perforation Behavior of Packaging Laminates, *J. Plast. Film Sheeting*, 2002, **18**, DOI: 10.1177/875608702033865.

41 K. H. Hu, *Measurements on the Resistance of Flexible Packaging Material to Puncture Abrasion and Flexure and the Relationship of these Measurments to the Performance of Packages Subjected to Conditions Causing Pinhole Formation*, 1973.

42 M. E. Evans and S. T. Hyde, *J. R. Soc., Interface*, 2011, **8**, 1274–1280.

43 S. M. Swartz and K. M. Middleton, *Cells Tissues Organs*, 2007, **187**, 59–84.

44 L. D. Landau and E. M. Lifshitz, *Theory of Elasticity*, 1970.

45 K. T. Wan, *J. Adhes.*, 1999, **70**, 209–219.

46 K. T. Wan, *J. Adhes.*, 1999, **70**, 197–207.

47 J. D. Glover, C. E. McLaughlin, M. K. McFarland and J. T. Pham, *J. Polym. Sci.*, 2020, **58**, 343–351.

48 C. Y. Hui, A. Jagota, S. J. Bennison and J. D. Londono, *Proc. R. Soc. A*, 2003, **459**, 1489–1516.

49 J. Liu, Z. Chen, X. Liang, X. Huang, G. Mao, W. Hong, H. Yu and S. Qu, Puncture mechanics of soft elastomeric membrane with large deformation by rigid cylindrical indenter, *J. Mech. Phys. Solids*, 2018, **112**, 458–471.

50 S. Steffensen, N. D. Madsen and H. M. Jensen, *Int. J. Solids Struct.*, 2013, **50**, 3406–3417.

51 X. Liu and G. K. German, *J. Mech. Behav. Biomed. Mater.*, 2015, **49**, 80–89.

52 S. Y. Chou, P. R. Krauss and P. J. Renstrom, *Appl. Phys. Lett.*, 1995, **67**, 3114.

53 L.-R. Bao, X. Cheng, X. D. Huang, L. J. Guo, S. W. Pang and A. F. Yee, *J. Vac. Sci. Technol., B: Microelectron. Nanometer Struct. – Process., Meas., Phenom.*, 2002, **20**, 2881.